A variational mechanics analysis of the stresses around breaks in embedded fibers

John A. Nairn

Department of Materials Science and Engineering, University of Utah, Salt Lake City, Utah 84112, USA

Embedded single-fiber tests are often used to characterize the fiber/matrix interface, but their interpretation is usually limited by reliance on the qualitative view of the stresses provided by shear-lag analyses. This paper describes a new, three-dimensional, axisymmetric solution for the stresses around breaks in embedded fibers. The new solution is obtained using variational mechanics. It obeys equilibrium and traction boundary conditions exactly, obeys compatibility approximately, includes all components of the stresses, accounts for interacting fiber breaks, and includes residual thermal stresses. We apply the stress analysis to the single-fiber fragmentation test. In some sample calculations, we plot all components of stress at the fiber/matrix interface and give predictions for an "ideal" single-fiber fragmentation test. The stress analysis technique is readily adaptable to new problems such as the single-fiber pull-out test, the microdrop debond test, the description of interfacial fracture or yielding, and the effect of interfacial friction.

1. Introduction

Without question, the fiber/matrix interface plays a role in determining composite properties. The relative importance of the interface is low or high depending on the specific property of interest. A complete understanding of composite materials can only follow from a thorough understanding of interfacial properties. To study the fiber/matrix interface, many researchers rely on embedded single-fiber tests. These tests include single-fiber fragmentation tests (Wadsworth and Spilling, 1968; Fraser, Ancker and DiBenedetto, 1975; Oshawa, Nakayama, Miwa and Hesegawa, 1978; Fraser, Ancker, DiBenedetto and Elbirli, 1983; Drzal, Rich, Camping and Park, 1980; Drzal, Rich and Lloyd, 1982; Drzal, Rich, Koenig and Lloyd, 1983; Drzal, Rich and Koenig, 1985; Rich and Drzal, 1986; Bascom and Jensen, 1986; Folkes and Wong, 1987; DiLandro and Pegoraro, 1987; DiLandro, DiBenedetto and Groeger, 1988; DiBenedetto and Lex, 1989; Netravali, Schwartz and Phoenix, 1989), fiber pull-out tests (Piggot, Chua and Andison, 1985; Piggot, 1987; Penn, Bystry and Marchionni, 1983), microindentation tests (Mandell, Chen and McGarry, 1980), and microdrop debond tests (Gaur and Miller, 1989). The results of these various tests are significant, but the quantitative interpretation of the results is limited by the near universal use of simplistic stress analyses such as shear-lag models (Cox, 1952; Rosen, 1964; Amirbayat and Hearle, 1969) or uniform shear stress assumptions (Kelly and Tyson, 1963). This paper introduces a new approach to the analysis of stresses in embedded fibers. The new analysis uses variational mechanics, achieves a closed-form solution, and is shown to be accurate.

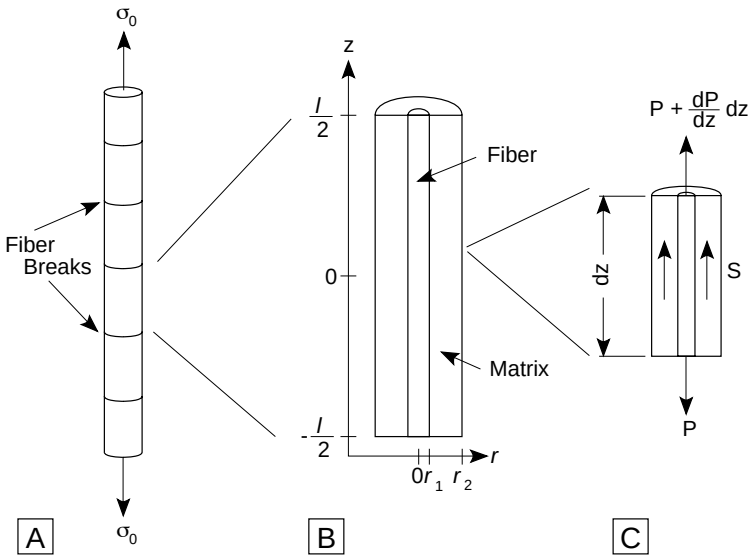

Fig. 1: The single-fiber fragmentation test. A: Under load σ_0, the single fiber develops multiple breaks which partitions the fiber into multiple fragments. B: A single fragment of length l showing a fiber of radius r_1 surrounded by a matrix cylinder of radius r_2. C: Force balance in a differential element of the fiber fragment.

Most analyses of stress transfer between a single fiber and a matrix can be classified as elasticity analyses, typically based on shear-lag (Cox, 1952; Rosen, 1964) or shear-lag equivalent (Amirbayat and Hearle, 1969) assumptions, or as elastic-plastic analyses, typically based on a constant interfacial shear stresses in regions where the interface has failed (Kelly and Tyson, 1963). The shear-lag elasticity analyses have their origins in the work of Cox (1952). As shown in Fig. 1C, the resultant shear force, S, that the matrix exerts on the fiber is

$$S = 2\pi r_1 \tau = \frac{dP}{dz} \tag{1}$$

where τ is the interfacial shear stress. Cox (1952) assumed that the shear force, S, is proportional to the difference between the displacement in the matrix, u, and the displacement in the matrix that would exist if the fiber were absent, v, or that $S = H(u - v)$. The resulting simple equation can be solved to give the tensile stress in the isolated fiber fragment of length l (See Fig. 1B). The result when the stresses at the fiber ends ($z = \pm l/2$) are zero is (Cox, 1952)

$$\sigma_f = E_A \varepsilon \left[1 - \frac{\cosh \beta z}{\cosh \frac{\beta l}{2}} \right] \tag{2}$$

Expressions of identical form have subsequently been derived by others (Rosen, 1964; Amirbayat and Hearle, 1969). The interfacial shear stress is

$$\tau = -\frac{1}{2} E_A \varepsilon r_1 \beta \frac{\sinh \beta z}{\cosh \frac{\beta l}{2}} \tag{3}$$

In these equations, E_A is the fiber axial modulus, ε is the applied strain, r_1 is the fiber radius and

$$\beta = \sqrt{\frac{H}{\pi r_1^2 E_A}} \tag{4}$$

A typical plot of the fiber tensile stress and the interfacial shear stress is in Fig. 2A. The tensile stress is zero at the fiber ends and builds to a constant value approaching $E_A\varepsilon$ near the center of the fragment. Stress

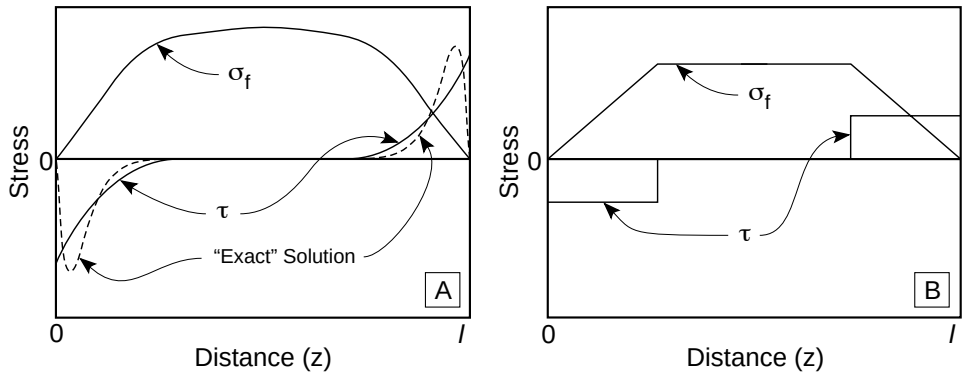

Fig. 2: Tensile stresses in the fiber (σ_f) and the shear stresses at the fiber/matrix interface (τ) as calculated by A: shear-lag analysis and B: constant shear stress analysis. Also shown in A is the form of the "exact" solution for the interfacial shear stresses.

is transferred from the matrix to the fiber by shear at the interface. The shear stress is a maximum at the fiber ends and decays towards zero at the center of the fragment.

There are limitations to the "simplistic" shear-lag analysis. First, the radial and hoop stresses are not determined by this one-dimensional analysis. These ignored stresses are important because they affect stress transfer as well as interfacial failure. In particular, the radial stress at the interface is important because differential thermal shrinkage between the fiber and the matrix typically leads to a shrink fit or radial compressive stresses at the fiber/matrix interface (Nairn, 1985). A compressive stress promotes physical adhesion and certainly plays a significant role in the performance of the interface. A second limitation is the necessity of determining the shear interaction parameter, H. Cox (1952) proposes that in the limit of high fiber volume fraction that

$$H = \frac{2\pi G_m}{\frac{r_2}{r_1} - 1} \approx \frac{2\pi G_m}{\ln \frac{r_2}{r_1}} \tag{5}$$

where G_m is the matrix shear modulus, and r_2 is the average separation between adjacent fibers. Embedded single-fiber tests are inherently low fiber volume fraction tests and Eq. (5) may poorly estimate H.

A third limitation with the shear-lag analysis is that it produces an inadmissible stress state, or a stress state that does not obey stress equilibrium (Whitney and Drzal, 1987). Consider analysis of the single-fiber fragmentation test in which the fiber contains multiple breaks (see Fig. 1A). The shear-lag solution predicts the maximum shear stress in any fragment to be at the fiber breaks. The "exact" solution, however, will have zero interfacial stress at the fiber breaks; zero shear is required by symmetry. Figure 2A compares the form of the "exact" solution to the shear-lag solution and shows that the shear-lag analysis misrepresents the interfacial shear stress, especially near the fiber breaks. We therefore question any conclusions about interfacial failure that are based on shear stress induced failure and that rely on the form of the shear stresses given by a shear-lag analysis

One way to avoid some limitations of the shear-lag analysis is to forget about the details of the interfacial shear stresses that lead to interfacial failure and only consider the post-failure stresses. Adopting this approach, Kelly and Tyson (1963) assumed the post-failure interfacial shear stress to be a constant, τ_y, characteristic of the strength of the fiber/matrix interface. Using this assumption and Eq. (1), the tensile stress in the fiber near a fiber break at $z = -l/2$ is

$$\sigma_f = \frac{2\tau_y}{r_1}\left(z + \frac{l}{2}\right) \tag{6}$$

The Kelly and Tyson approach is elastic-plastic in that the fiber stress will increase linearly (according to Eq. (6)) until it reaches $E_A\varepsilon$ or the tensile stress that would exist in the absence of the fiber break. After reaching $E_A\varepsilon$, the tensile stress is assumed to remain constant. A similar analysis applies to the stresses near the fiber end at $z = l/2$. The interfacial shear stress and the fiber tensile stress by this model are shown in Fig. 2B.

The constant shear-stress approach also has limitations. First, this one-dimensional approach still does not define the hoop or radial stresses and therefore again ignores the important interfacial radial stress. In the post-failure state, a large contribution to τ_y might come from friction and the amount of frictional force will depend on the magnitude of the radial compressive stresses. Second, this approach only seeks to describe the stresses in the post-failure state. As such, it does not help in understanding interfacial failure mechanisms.

There have been a few finite element analyses of stresses around breaks in embedded single fibers (Carrara and McGarry, 1968; Broutman and Agarwal, 1974) but there has been surprisingly little effort at achieving analytical methods that improve on the shear-lag methods. One significant result is described by Whitney and Drzal (1987). They use a stress function approach that guarantees an admissible solution. Their results, however, have two limitations. First, their choice of a stress function was guided by the previously discussed shear-lag solutions. There is unfortunately no way to judge the accuracy of this approach. A better approach, as done in this paper, is to choose a stress function that minimizes complementary energy. By the principle of variational mechanics this approach assures us of finding the most accurate solution for a given set of assumptions. Second, their analysis only deals with an isolated fiber break. In real single-fiber fragmentation tests, the breaks interact and the stress analysis should include this effect.

The goal of this paper is to improve the analysis and interpretation of embedded single fiber tests. To avoid the limitations of the shear-lag model or the Whitney and Drzal (1987) approach, and to avoid the burdens of purely numerical solutions, we present a new closed-form, three-dimensional, axisymmetric solution for the stresses around breaks in an embedded single fiber. We specifically discuss the single-fiber fragmentation test (Fig. 1A) which can be viewed as a two phase structure containing a matrix phase and a fiber phase. Upon loading, the brittle fiber phase fails in a roughly periodic array of cracks. There is a close analogy between this structure and symmetric cross-ply laminates of generic layup $[0_m/90_n/0_m]$. The cross-ply laminate can also be viewed as a two phase structure consisting of a 0° ply phase and a 90° ply phase. Upon loading, the brittle 90° ply phase fails in a nearly periodic array of cracks (Hahn and Tsai, 1974; Garret and Bailey, 1977; Highsmith and Reifsnider, 1982). Because of the analogy between failure of embedded single fibers and cross-ply laminates, we can adapt some of the stress analysis techniques for cross-ply laminates to the analysis of stresses in embedded single fibers. The most rigorous, closed-form analysis of stresses in cross-ply laminates is the recent variational mechanics analysis developed by Hashin (1985; 1986) that has been extended to cover thermal stresses and the analysis of 90° ply cracking (Nairn, 1989; Liu and Nairn, 1990; Liu and Nairn, 1992). The variational mechanics analysis for embedded single fibers parallels Hashin's (1985; 1986) and related analyses (Nairn, 1989; Liu and Nairn, 1990; Liu and Nairn, 1992). The major difference is that the cross-ply laminate analysis is a two-dimensional analysis and the embedded single fiber analysis is a three-dimensional, axisymmetric analysis.

This new variational mechanics analysis has many features. The analysis begins with an admissible stress state that obeys equilibrium and traction boundary conditions exactly. An approximate, but demonstrably

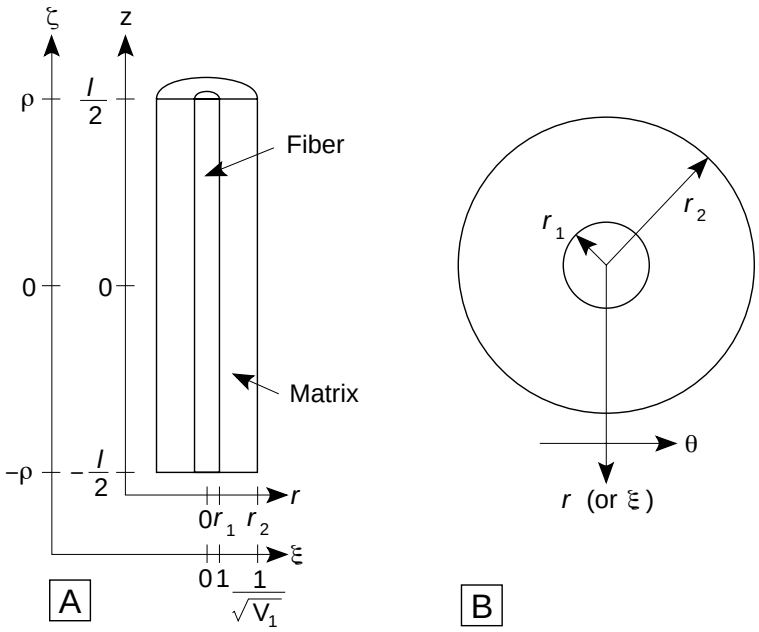

Fig. 3: The two-cylinder model used for the axisymmetric stress analysis. A single fragment of length l showing the axial and radial coordinates in both dimensioned and dimensionless forms. B: A cross-section of the two- cylinder model showing the fiber of radius r_1 and the matrix of radius r_2.

accurate form of the stress state is found by minimizing the complementary energy. In the final result, all stresses are included and the solution can be used for any fiber volume fraction. We analyze an entire fiber fragment and thus the solution accounts for interacting fiber breaks. Finally, the solution includes residual thermal stresses and therefore can be used to assess the role of radial compressive stresses on interfacial properties. The next section describes the variational mechanics analysis of the single-fiber fragmentation specimen for a transversely isotropic fiber in an isotropic matrix of any volume fraction. The analysis assumes the fiber and the matrix are linear elastic and that the interfacial adhesion is perfect. In the results section, we plot the stresses at the fiber/matrix interface and give predictions for an "ideal" single-fiber fragmentation test. The analysis presented in this paper is only intended as a starting point for the analysis of single embedded fiber tests. The discussion section describes how the analysis can include imperfect adhesion, account for interfacial friction effects, and handle other single-fiber tests such as microdrop debond tests (Gaur and Miller, 1989).

2. Stress Analysis

2.1. The Stress Function and an Admissible Stress State.

We consider the two concentric cylinders in Fig. 3. The inner solid cylinder is the fiber and the outer hollow cylinder is the surrounding matrix. The radii of the two cylinders are r_1 and r_2. During a single-fiber fragmentation test, the central cylinder will fracture and become partitioned into a series of fragments. The fiber breaks do not disturb the axisymmetric nature of the stresses and we thus conduct a three-dimensional, axisymmetric stress analysis of the single fiber fragment of length l (Fig. 3A).

For axially symmetric stress states, the shear stresses $\tau_{r\theta}$ and $\tau_{z\theta}$ are zero and we only need to consider the remaining stresses — σ_{rr}, $\sigma_{\theta\theta}$, σ_{zz}, and τ_{rz}. The equations of equilibrium for the four remaining stresses

reduce to (Timoshenko and Goodier, 1970)

$$\frac{\partial \sigma_{rr}}{\partial r} + \frac{\partial \tau_{rz}}{\partial z} + \frac{\sigma_{rr} - \sigma_{\theta\theta}}{r} = 0 \tag{7}$$

$$\frac{\partial \tau_{rz}}{\partial r} + \frac{\partial \sigma_{zz}}{\partial z} + \frac{\tau_{rz}}{r} = 0 \tag{8}$$

We rewrite τ_{rz} and σ_{rr} using two functions of r and z, Ω and Ψ, as

$$\tau_{rz} = -\frac{\partial^2 \Psi}{\partial r \partial z} \tag{9}$$

$$\sigma_{rr} = \frac{1}{r}\frac{\partial \Omega}{\partial r} + \frac{\partial^2 \Psi}{\partial z^2} \tag{10}$$

Integrating the equations of equilibrium we find

$$\sigma_{\theta\theta} = \frac{\partial^2 \Omega}{\partial r^2} + \frac{\partial^2 \Psi}{\partial z^2} \tag{11}$$

$$\sigma_{zz} = \frac{\partial^2 \Psi}{\partial r^2} + \frac{1}{r}\frac{\partial \Psi}{\partial r} \tag{12}$$

We introduce one and only one assumption — we assume that σ_{zz} within each cylinder depends only on the z coordinate. All such stress states are recovered by selecting

$$\Psi(r,z) = \frac{r^2 \psi_0}{4} + \psi_1 \ln r + \psi_2 \tag{13}$$

where ψ_0, ψ_1, and ψ_2 are arbitrary functions of z only. To get σ_{rr} and $\sigma_{\theta\theta}$ we need to know Ω which we find using radial compatibility. In axially symmetric stress states (Timoshenko and Goodier, 1970)

$$\varepsilon_{rr} = \frac{\partial u}{\partial r} \qquad \text{and} \qquad \varepsilon_{\theta\theta} = \frac{u}{r} \tag{14}$$

which leads to the compatibility condition

$$\frac{\varepsilon_{rr} - \varepsilon_{\theta\theta}}{r} = \frac{\partial \varepsilon_{\theta\theta}}{\partial r} \tag{15}$$

When each cylinder is at least transversely isotropic with the axial direction along the cylinder axis and σ_{zz} is independent of r, Eq. (15) reduces to

$$(1 + \nu_T)\frac{\sigma_{rr} - \sigma_{\theta\theta}}{r} = \frac{\partial}{\partial r}(\sigma_{\theta\theta} - \nu_T \sigma_{rr}) \tag{16}$$

where $\nu_T = \nu_{r\theta} = \nu_{\theta r}$ is the transverse Poisson's ratio. In terms of Ω and Ψ, Eq. (16) is

$$\frac{\partial}{\partial r}\left(\frac{1}{r}\frac{\partial \Omega}{\partial r} + \frac{\partial^2 \Omega}{\partial r^2} + (1 - \nu_T)\frac{\partial^2 \Psi}{\partial z^2}\right) = 0 \tag{17}$$

This equation is solved in the general sense by putting

$$\Omega = -(1 - \nu_T)\left[\frac{r^4}{64}\psi_0'' + \frac{r^2 \ln r}{4}\psi_1'' + \frac{r^2}{4}\psi_2'' + \frac{r^2}{4}\psi_3 + \psi_4 \ln r + \psi_5\right] \tag{18}$$

where ψ_3, ψ_4, and ψ_5 are three new arbitrary functions of z only. Using Ω, the general axially symmetric stress state in which σ_{zz} is independent of r becomes

$$\sigma_{zz} = \psi_0 \tag{19}$$

$$\tau_{rz} = -\frac{r\psi_0'}{2} - \frac{\psi_1'}{r} \tag{20}$$

$$\sigma_{rr} = \frac{r^2}{16}\psi_0''(3+\nu_T) + \frac{\psi_1''}{4}\big(2(1+\nu_T)\ln r + (1-\nu_T)\big) + \psi_2 - \frac{\psi_4}{r^2} \tag{21}$$

$$\sigma_{\theta\theta} = \frac{r^2}{16}\psi_0''(1+3\nu_T) + \frac{\psi_1''}{4}\big(2(1+\nu_T)\ln r - (1-\nu_T)\big) + \psi_2 + \frac{\psi_4}{r^2} \tag{22}$$

where ψ_2 and ψ_4 have been redefined. In terms of the previous functions $\psi_2 = \psi_2'' - \frac{(1-\nu_T)}{2}(\psi_1'' + \psi_2'' + \psi_3)$ and $\psi_4 = (1-\nu_T)\psi_4$.

We apply the general stress function to each cylinder separately. We denote the arbitrary functions of z defined in the previous paragraph by $\psi_{i,j}$ where i is 0, 1, 2, or 4 denoting the function number and j is 1 for the fiber cylinder or 2 for the matrix cylinder. In the fiber cylinder, the requirement for finite stresses at $r = 0$ forces $\psi_{4,1} = \psi_{1,1}' = \psi_{1,1}'' = 0$. In the matrix cylinder we have boundary conditions

$$\tau_{rz,2}(r_2) = 0 \tag{23}$$

$$\sigma_{rr,2}(r_1) = \sigma_{rr,1}(r_1) \tag{24}$$

$$\sigma_{rr,2}(r_2) = \sigma_{edge} \tag{25}$$

where σ_{edge} is a constant applied radial stress. By force balance

$$V_1\sigma_{zz,1} + V_2\sigma_{zz,2} = \sigma_0 \tag{26}$$

where σ_0 is the total applied axial stress and V_1 and $V_2 = 1 - V_1$ are the volume fractions of the fiber and matrix, respectively. From these conditions, the stresses in the fiber become

$$\sigma_{zz,1} = \psi \tag{27}$$

$$\tau_{rz,1} = -\frac{\xi\psi'}{2} \tag{28}$$

$$\sigma_{rr,1} = \frac{\psi''}{16}\left(\xi^2(3+\nu_T) + \nu_m - \nu_T + \frac{2(1+\nu_m)\ln V_1}{V_2}\right) - \frac{\psi_{4,2}V_2}{r_2^2V_1} + \sigma_{edge} \tag{29}$$

$$\sigma_{\theta\theta,1} = \frac{\psi''}{16}\left(\xi^2(1+3\nu_T) + \nu_m - \nu_T + \frac{2(1+\nu_m)\ln V_1}{V_2}\right) - \frac{\psi_{4,2}V_2}{r_2^2V_1} + \sigma_{edge} \tag{30}$$

and the stresses in the matrix become

$$\sigma_{zz,2} = \frac{\sigma_0}{V_2} - \frac{V_1\psi}{V_2} \tag{31}$$

$$\tau_{rz,2} = \frac{\psi' V_1}{2V_2}\left(\xi - \frac{1}{\xi V_1}\right) \tag{32}$$

$$\sigma_{rr,2} = \frac{\psi''}{16V_2}\left[(3+\nu_m) + 2(1+\nu_m)\ln\xi^2V_1 - \xi^2V_1(3+\nu_m)\right] + \frac{\psi_{4,2}}{r_2^2}\left(1 - \frac{1}{\xi^2V_1}\right) + \sigma_{edge} \tag{33}$$

$$\sigma_{\theta\theta,2} = \frac{\psi''}{16V_2}\left[(5\nu_m - 1) + 2(1+\nu_m)\ln\xi^2V_1 - \xi^2V_1(1+3\nu_m)\right] + \frac{\psi_{4,2}}{r_2^2}\left(1 + \frac{1}{\xi^2V_1}\right) + \sigma_{edge} \tag{34}$$

In these equations $\psi = \psi_{0,1}$, ν_m is the Poisson's ratio of the isotropic matrix, and ν_T is the transverse Poisson's ratio of the fiber. The stresses have been put in a dimensionless form in which $\xi = \frac{r}{r_1}$ and ψ and $\psi_{4,2}$ are functions of the dimensionless axial coordinate $\zeta = \frac{z}{r_1}$.

We eliminate $\psi_{4,2}$ by requiring radial displacement, $u = r\varepsilon_{\theta\theta}$, to be continuous at the fiber matrix interface. The resulting calculation yields

$$\frac{\psi_{4,2}}{r_2^2} = \frac{A_1}{A_0}\frac{\psi''}{16} + \frac{A_2}{A_0}\sigma_{edge} + \frac{A_3}{A_0}\psi + \frac{A_4}{A_0}\sigma_0 + \frac{A_5}{A_0}T \tag{35}$$

where

$$A_0 = \frac{V_2(1-\nu_T)}{V_1E_T} + \frac{1-\nu_m}{E_m} + \frac{1+\nu_m}{V_1E_m} \tag{36}$$

$$A_1 = \left(\frac{1-\nu_T}{E_T} - \frac{1-\nu_m}{E_m}\right)(1+\nu_m)\left(1 + \frac{2\ln V_1}{V_2}\right) + \frac{2(1-\nu_m)}{V_2E_m} \tag{37}$$

$$A_2 = \frac{1-\nu_T}{E_T} - \frac{1-\nu_m}{E_m} \tag{38}$$

$$A_3 = -\left(\frac{\nu_A}{E_A} + \frac{V_1\nu_m}{V_2E_m}\right) \tag{39}$$

$$A_4 = \frac{\nu_m}{V_2E_m} \tag{40}$$

$$A_5 = \alpha_T - \alpha_m \tag{41}$$

In these equations, E_A and E_T are the axial and transverse moduli of the fiber, E_m is the modulus of the matrix, $\nu_A = \nu_{zr} = \nu_{z\theta}$ is the axial Poisson's ratio of the fiber, ν_m is the Poisson's ratio of the matrix α_T is the transverse thermal expansion coefficient of the fiber, α_m is the thermal expansion coefficient of the matrix, and $T = T_s - T_0$ is the temperature difference between the specimen temperature, T_s, and the stress-free temperature, T_0.

We next make a general observation about these stresses which will lead us to a requirement for a third cylinder. When a crack develops in the fiber, the stress $\sigma_{zz,1}$ and hence ψ at the crack are zero. From Eq. (31) the tensile stress in the matrix will increase to $\sigma_{zz,2} = \sigma_0/V_2$. By the assumptions inherent in the stress state (i.e., σ_{zz} independent of r), this stress concentration in the matrix will exist near the crack tip and continue unabated out to the edge of the matrix at $r = r_2$. This behavior of the σ_{zz} stresses will not cause serious errors when V_1 is fairly large. When the fiber volume fraction gets small (*e.g.*, fiber in an infinite matrix), however, we can expect this enforced r independence to give poor results. More realistically, we would expect that the stress concentration due to a fiber break will be felt only for some finite distance into the matrix. If the effect of the fiber break is apparent for $r \le r_c$ where r_c is some critical radius, then the stresses in the matrix beyond r_c should be the far-field stresses or the stresses in the matrix that exist when the fiber has no breaks.

A major interest in embedded single-fiber tests is for fibers in an infinite matrix. When the matrix is infinite, we account for the form of the stresses described in the previous paragraph by adding a third cylinder of infinite radius. The stresses in the third cylinder are set to the far-field matrix stresses. We find these far-field stresses using a two cylinder analysis that has an infinite radius matrix cylinder, a fiber with no breaks, and $\sigma_{edge} = 0$. The calculation is given in Appendix 1. The stresses in the third cylinder or far-field matrix cylinder simplify to:

$$\sigma_{zz,3} = \sigma_{app} \tag{42}$$

$$\tau_{rz,3} = 0 \tag{43}$$

$$\sigma_{rr,3} = \frac{\sigma_\infty}{\xi^2} \tag{44}$$

$$\sigma_{\theta\theta,3} = -\frac{\sigma_\infty}{\xi^2} \tag{45}$$

where σ_{app} is the total applied stress and σ_∞ is the radial stress at $\xi = 1$. An explicit expression for σ_∞ is given in Appendix 1.

With the addition of a third cylinder, we must make changes in the previous two-cylinder model. The two required changes relate to the axial and radial boundary conditions. First, the third cylinder applies a radial stress on the inner two cylinders. This constant radial stress can easily be incorporated into the two-cylinder model because we anticipated it by allowing a non-zero edge stress. From Eq. (44), we simply set $\sigma_{edge} = V_1\sigma_\infty$. Note that even in the presence of the third cylinder, we continue to reference volume fractions to the two inner cylinders. Thus, $V_1 + V_2 = 1$ and $V_3 = \infty$. Second, the third cylinder will affect σ_0. The appropriate value of σ_0 is the one that causes the total axial displacement of the two inner cylinders to match the total axial displacement of the third cylinder. σ_0 is a function of the fragment aspect ratio $\left(\rho = \frac{l}{2r_1}\right)$ and will be evaluated after we determine the stresses. For now, we indicate the functional dependence of σ_0 by writing it as $\sigma_0(\rho)$

For subsequent calculation, it is useful to rewrite the stresses in the two inner cylinders in a matrix form. The stress in cylinder i is given by $[\sigma_i] = [B_i][\psi]$ where $[\sigma_i] = (\sigma_{rr,i}, \sigma_{\theta\theta,i}, \sigma_{zz,i}, \tau_{rz,i})$, $[\psi] = (\sigma_0(\rho), T, \psi, \psi', \psi'', \sigma_\infty)$, and $[B_i]$ is a matrix specific for each component. For the fiber cylinder:

$$[B_1] = \begin{pmatrix} -\frac{V_2A_4}{V_1A_0} & -\frac{V_2A_5}{V_1A_0} & -\frac{V_2A_3}{V_1A_0} & 0 & f_1 & V_1\left(1-\frac{V_2A_2}{V_1A_0}\right) \\ -\frac{V_2A_4}{V_1A_0} & -\frac{V_2A_5}{V_1A_0} & -\frac{V_2A_3}{V_1A_0} & 0 & f_2 & V_1\left(1-\frac{V_2A_2}{V_1A_0}\right) \\ 0 & 0 & 1 & 0 & 0 & 0 \\ 0 & 0 & 0 & -\frac{\xi}{2} & 0 & 0 \end{pmatrix} \tag{46}$$

where

$$f_1 = \frac{1}{16}\left(\xi^2(3+\nu_T) + \nu_m - \nu_T + \frac{2(1+\nu_m)\ln V_1}{V_2} - \frac{V_2A_1}{V_1A_0}\right) \tag{47}$$

$$f_2 = \frac{1}{16}\left(\xi^2(1+3\nu_T) + \nu_m - \nu_T + \frac{2(1+\nu_m)\ln V_1}{V_2} - \frac{V_2A_1}{V_1A_0}\right) \tag{48}$$

For the near-field matrix cylinder (cylinder 2):

$$[B_2] = \begin{pmatrix} \frac{A_4}{A_0}\left(1-\frac{1}{\xi^2V_1}\right) & \frac{A_5}{A_0}\left(1-\frac{1}{\xi^2V_1}\right) & \frac{A_3}{A_0}\left(1-\frac{1}{\xi^2V_1}\right) & 0 & f_3 & V_1\left[1+\frac{A_2}{A_0}\left(1-\frac{1}{\xi^2V_1}\right)\right] \\ \frac{A_4}{A_0}\left(1+\frac{1}{\xi^2V_1}\right) & \frac{A_5}{A_0}\left(1+\frac{1}{\xi^2V_1}\right) & \frac{A_3}{A_0}\left(1+\frac{1}{\xi^2V_1}\right) & 0 & f_4 & V_1\left[1+\frac{A_2}{A_0}\left(1+\frac{1}{\xi^2V_1}\right)\right] \\ \frac{1}{V_2} & 0 & -\frac{V_1}{V_2} & 0 & 0 & 0 \\ 0 & 0 & 0 & \frac{V_1}{2V_2}\left(\xi-\frac{1}{\xi V_1}\right) & 0 & 0 \end{pmatrix} \tag{49}$$

where

$$f_3 = \frac{1}{16V_2}\left[(3+\nu_m)\left(1-\xi^2V_1\right) + 2(1+\nu_m)\ln\xi^2V_1 + \frac{V_2A_1}{A_0}\left(1-\frac{1}{\xi^2V_1}\right)\right] \tag{50}$$

$$f_4 = \frac{1}{16V_2}\left[(1+3\nu_m)\left(1-\xi^2V_1\right) - 2(1-\nu_m) + 2(1+\nu_m)\ln\xi^2V_1 + \frac{V_2A_1}{A_0}\left(1+\frac{1}{\xi^2V_1}\right)\right] \tag{51}$$

2.2. Complementary Energy Minimization

The three cylinder stress state is completely defined by one unknown function — ψ. The stress state is an admissible stress state in that it obeys stress equilibrium, traction boundary conditions, and interface stress continuity. By the principal of minimum complementary energy, the function ψ that produces the minimum value for the complementary energy will give the best approximation to the stresses in an embedded single fiber. For thermoelastic analyses, the complementary energy can be minimized by minimizing the functional Γ given by

$$\Gamma = \int_V \frac{1}{2}[\sigma][K][\sigma]dV + \int_V [\sigma]\cdot[\alpha]TdV - \int_{S_1}[\sigma]\cdot\hat{u}dS \tag{52}$$

where $[K]$ is the compliance tensor, $[\alpha]$ is the thermal expansion coefficient tensor, V is total volume, and S_1 is that part of the specimen surface subjected to fixed displacement of $\hat{u}$ (Carlson, 1984). For the problems discussed in this paper, S_1 is null.

We evaluate Γ for the region between the two cracks located at $z = \pm l/2$ (see Fig. 3A):

$$\Gamma = \sum_{i=1}^{3}\int_0^{2\pi} d\theta \int_{r_{0i}}^{r_{fi}} rdr \int_{-\frac{l}{2}}^{\frac{l}{2}} dz \left(\frac{1}{2}[\psi]^T[B_i]^T[K_i][B_i][\psi_i] + T[\alpha_i]\cdot[B_i][\psi]\right) \tag{53}$$

where r_{0i} and r_{fi} are the initial and final radii of cylinder i. When each cylinder is at least orthotropic with the symmetry axes of the orthotropy coincident with the axisymmetry, the symmetric compliance tensor is

$$[K_i] = \begin{pmatrix} K_{11}^{(i)} & K_{12}^{(i)} & K_{13}^{(i)} & 0 \\ K_{12}^{(i)} & K_{22}^{(i)} & K_{23}^{(i)} & 0 \\ K_{13}^{(i)} & K_{23}^{(i)} & K_{33}^{(i)} & 0 \\ 0 & 0 & 0 & K_{44}^{(i)} \end{pmatrix} \tag{54}$$

and the thermal expansion coefficient tensor is

$$[\alpha_i] = (\alpha_{11}^{(i)}, \alpha_{22}^{(i)}, \alpha_{33}^{(i)}, 0) \tag{55}$$

where the 1, 2, and 3 coordinates refer to r, θ, and z direction properties and the superscript (i) denotes the properties in cylinder i. Because of axisymmetry, the θ integrals are trivially 2π. Doing the θ integrals, collecting the r integrals, and recasting in dimensionless form results in

$$\Gamma = \pi r_1^3 \int_{-\rho}^{\rho} d\zeta \left([\psi]^T[C][\psi] + 2T[D][\psi]\right) \tag{56}$$

where

$$[C] = \sum_{i=1}^{3}\int_{\xi_{0i}}^{\xi_{fi}} \xi d\xi [B_i]^T[K_i][B_i] \tag{57}$$

$$[D] = \sum_{i=1}^{3}\int_{\xi_{0i}}^{\xi_{fi}} \xi d\xi [\alpha_i][B_i] \tag{58}$$

The matrix $[C]$ is 6×6 and the vector $[D]$ is of length 6. The new dimensionless quantities are defined as $\xi_{0i} = \frac{r_{0i}}{r_1}$ and $\xi_{0f} = \frac{r_{0f}}{r_1}$

In evaluating the symmetric $[C]$ matrix and the $[D]$ vector, C_{14}, C_{24}, C_{34}, C_{45}, C_{46}, and D_4 are obviously zero. Some simple integrations reveal that C_{12}, C_{23}, C_{25}, and C_{26} are also zero and that $C_{22} = -D_2$. Expanding Eq. (56) therefore results in

$$\Gamma = \Gamma_0 + \pi r_1^3 \int_{-\rho}^{\rho} d\zeta \Big(C_{33}\psi^2 + 2C_{35}\psi\psi'' + C_{55}\psi''^2 + C_{44}\psi'^2 + 2(C_{13}\sigma_0(\rho) + C_{36}\sigma_\infty + D_3T)\psi + 2(C_{15}\sigma_0(\rho) + C_{56}\sigma_\infty + D_5T)\psi'' \Big) \tag{59}$$

where Γ_0 is a constant and will not enter the minimization procedure:

$$\Gamma_0 = 2\pi\rho r_1^3 \Big(C_{11}\sigma_0(\rho)^2 + 2C_{16}\sigma_0(\rho)\sigma_\infty + C_{66}\sigma_\infty^2 + 2TD_1\sigma_0(\rho) + 2D_6T\sigma_\infty + D_2T^2 \Big) \tag{60}$$

The elements of the $[C]$ matrix and the $[D]$ vector all involve integrations over the dimensionless radial coordinate ξ. The integrations can all be evaluated in closed form. When the fiber is transversely isotropic with the unique axis along the fiber axis and the matrix is isotropic, the result of much tedious algebra yields:

$$C_{33} = \frac{1}{2}\left(\frac{1}{E_A} + \frac{V_1}{V_2E_m}\right) - \frac{V_2A_3^2}{V_1A_0} \tag{61}$$

$$C_{35} = \frac{1}{16}\left[A_3\left[(1+\nu_m)\left(1+\frac{2\ln V_1}{V_2}\right) - \frac{V_2A_1}{V_1A_0}\right] - 2A_4\right] \tag{62}$$

$$C_{55} = \frac{1}{256}\left\{\frac{1-\nu_T}{E_T}\left[\frac{5+2\nu_T}{3} + \nu_m(2+\nu_m)\right] + \frac{4A_2(1+\nu_m)^2\ln V_1}{V_2}\left(1+\frac{\ln V_1}{V_2}\right) - \frac{V_2A_1^2}{V_1A_0} + \frac{1-\nu_m}{E_m}\left[\frac{V_2^2(1+\nu_m)(5+3\nu_m) - 3V_2(1+\nu_m)(3+\nu_m) + 6(5+3\nu_m)}{3V_1V_2} + \frac{8(1+\nu_m)\ln V_1}{V_2^2}\right]\right\} \tag{63}$$

$$C_{44} = \frac{1}{16}\left[\frac{1}{G_A} - \frac{1}{G_m}\left(1+\frac{2}{V_2}+\frac{2\ln V_1}{V_2^2}\right)\right] \tag{64}$$

$$C_{13} = -\frac{1}{2V_2E_m} - \frac{V_2A_3A_4}{V_1A_0} \tag{65}$$

$$C_{36} = -\frac{V_2A_3A_2}{A_0} - V_1\left(\frac{\nu_A}{E_A} - \frac{\nu_m}{E_m}\right) \tag{66}$$

$$D_3 = -\frac{V_2A_3}{V_1A_0}\left[\alpha_T - \alpha_m\right] + \frac{1}{2}\left[\alpha_A - \alpha_m\right] \tag{67}$$

where the new terms, G_A and G_m, are the axial shear modulus of the fiber and the shear modulus of the matrix, respectively. The constants not listed above are not required for the calculations in this paper.

We begin with a limiting solution that ignores end effects and therefore applies to the stresses far from fiber breaks. Far from the fiber breaks the shear stresses will be zero which implies that $\psi' = \psi'' = 0$ which further implies that ψ is a constant. The constant will depend on ρ and we denote it as $\psi_0(\rho)$. Γ is easily evaluated to be

$$\Gamma = \Gamma_0 + 2\pi r_1^3\rho\left[C_{33}\psi_0(\rho)^2 + +2(C_{13}\sigma_0(\rho) + C_{36}\sigma_\infty + D_3T)\psi_0(\rho)\right] \tag{68}$$

Γ is minimized when

$$\psi_0(\rho) = -\frac{C_{13}\sigma_0(\rho) + C_{36}\sigma_\infty + D_3T}{C_{33}} \tag{69}$$

Because the one assumption about σ_{zz} being independent of r is correct far from the ends, the value of $\psi_0(\rho)$ should, and does, recover the exact solution for a two-cylinder model under axial stress $\sigma_0(\rho)$ and radial stress $V_1\sigma_\infty$ in which the fiber has no breaks (see Appendix 1).

A special case of the limiting solution is for an intact fiber in an infinite matrix. For this case the stresses in the near-field matrix must match the stresses in the far-field matrix. Defining

$$\psi_\infty = \lim_{\rho\to\infty} \psi_0(\rho) \tag{70}$$

we require

$$\sigma_{zz,2} = \sigma_{app} = \frac{\sigma_0(\infty) - V_1\psi_\infty}{V_2} \tag{71}$$

Solving for $\sigma_0(\infty)$ and substituting into Eq. (69) results in

$$\psi_\infty = -\frac{C_{13}V_2\sigma_{app} + C_{36}\sigma_\infty + D_3T}{C_{33} + V_1C_{13}} \tag{72}$$

Eq. (72) recovers the exact elasticity result in Appendix 1.

To find the stresses near the breaks in a fiber fragment of length l, we minimize Γ using the calculus of variations. The Euler equation for ψ is

$$\psi^{iv} + p\psi'' + q\psi = q\psi_0(\rho) \tag{73}$$

where

$$p = \frac{2C_{35} - C_{44}}{C_{55}} \qquad\qquad q = \frac{C_{33}}{C_{55}} \tag{74}$$

Because $\psi_0(\rho)$ is obviously a particular solution to the Euler equation, we can write the general solution as $\psi = \psi_0(\rho)(1-\phi)$ where ϕ is the solution to the homogeneous equation

$$\phi^{iv} + p\phi'' + q\phi = 0 \tag{75}$$

The requirement that $\sigma_{zz,1}(\pm l) = \tau_{rz,1}(\pm l) = 0$ or that the the fiber fracture surfaces are traction free leads to the boundary conditions $\phi(\pm\rho) = 1$ and $\phi'(\pm\rho) = 0$. Eq. (75) and its boundary conditions are identical to the equation and boundary conditions that appeared in the analysis of the stresses in cross-ply laminates (Hashin, 1985; Hashin, 1986; Nairn, 1989). The solution extracted from Nairn (1989) is

$$\phi = \frac{\frac{\beta\cosh\alpha\zeta}{\sinh\alpha\rho} - \frac{\alpha\cosh\beta\zeta}{\sinh\beta\rho}}{\beta\coth\alpha\rho - \alpha\coth\beta\rho} \tag{76}$$

where

$$\alpha = \sqrt{-\frac{p}{2} + \sqrt{\frac{p^2}{4} - q}} \tag{77}$$

$$\beta = \sqrt{-\frac{p}{2} - \sqrt{\frac{p^2}{4} - q}} \tag{78}$$

This solution assumes that $\frac{p^2}{4} - q > 0$ which holds for the calculations in this paper. For completeness, the solution when $\frac{p^2}{4} - q < 0$ is provided in Appendix 2.

Having determined the stresses we can find $\sigma_0(\rho)$ by equating total displacement of the near-field matrix cylinder (cylinder 2) to the far-field matrix cylinder (cylinder 3). Integrating the strains we have

$$\int_{-\frac{l}{2}}^{\frac{l}{2}} \varepsilon_{zz,3}dz = \int_{-\frac{l}{2}}^{\frac{l}{2}} \varepsilon_{zz,2}dz \tag{79}$$

Inserting the stresses, noting that $\int_{-\rho}^{\rho}\psi''d\zeta = 0$, and using the definition of $\psi_0(\rho)$ in Eq. (69), we quickly achieve

$$\sigma_0(\rho) = \frac{\sigma_{app} + \left(2\nu_m V_1\left(1+\frac{A_2}{A_0}\right) + \frac{2V_1E_mC_{36}C_{13}(1-\langle\phi\rangle)}{C_{33}}\right)\sigma_\infty + \left(\frac{2\nu_m A_5}{A_0} + \frac{2V_1E_mD_3C_{13}(1-\langle\phi\rangle)}{C_{33}}\right)T}{\frac{1}{V_2} - \frac{2\nu_m A_4}{A_0} - \frac{2V_1E_mC_{13}^2(1-\langle\phi\rangle)}{C_{33}}} \tag{80}$$

Eq. (80) requires evaluation of $\langle\phi\rangle$ defined as

$$\langle\phi\rangle = \frac{1}{2\rho}\int_{-\rho}^{\rho}\phi d\zeta \tag{81}$$

We could evaluate this term by integration of ϕ, but it is simpler to integrate Eq. (75) and rearrange to get

$$\langle\phi\rangle = -\frac{\phi'''(\rho)}{\rho q} = \frac{\chi(\rho)}{\rho q} \tag{82}$$

where we have defined a new function

$$\chi(\rho) = -\phi'''(\rho) = \alpha\beta(\beta^2-\alpha^2)\frac{\tanh\alpha\rho\tanh\beta\rho}{\beta\tanh\beta\rho - \alpha\tanh\alpha\rho} \tag{83}$$

In evaluating specific stresses we need to know the first and second derivatives of ψ. From Eq. (74), $\psi' = -\psi_0(\rho)\phi'$ and $\psi'' = -\psi_0(\rho)\phi''$ where

$$\phi' = \alpha\beta\frac{\frac{\sinh\alpha\zeta}{\sinh\alpha\rho} - \frac{\sinh\beta\zeta}{\sinh\beta\rho}}{\beta\coth\alpha\rho - \alpha\coth\beta\rho} \tag{84}$$

$$\phi'' = \alpha\beta\frac{\frac{\alpha\cosh\alpha\zeta}{\sinh\alpha\rho} - \frac{\beta\cosh\beta\zeta}{\sinh\beta\rho}}{\beta\coth\alpha\rho - \alpha\coth\beta\rho} \tag{85}$$

A special case of the above solution is the stress state around an isolated fiber break. We find these stresses by taking the limit as $\rho\to\infty$. Taking this limit and redefining ζ such that the origin is at the crack rather than midway between two cracks gives the following results:

$$\psi = \psi_\infty\left[1 - \frac{1}{\beta-\alpha}\left(\beta e^{-\alpha\zeta} - \alpha e^{-\beta\zeta}\right)\right] \tag{86}$$

$$\psi' = \frac{\psi_\infty\alpha\beta}{\beta-\alpha}\left(e^{-\alpha\zeta} - e^{-\beta\zeta}\right) \tag{87}$$

$$\psi'' = -\frac{\psi_\infty\alpha\beta}{\beta-\alpha}\left(\alpha e^{-\alpha\zeta} - \beta e^{-\beta\zeta}\right) \tag{88}$$

Table 1
Typical mechanical properties for a carbon fiber and an epoxy. These properties are used for the sample calculations in the Results section.

Property	Carbon Fiber	Epoxy Matrix
E_A or E_m (MPa)	220000	4300
E_T (MPa)	14000	
G_A or G_m (MPa)	35000	1605
ν_A or ν_m	0.2	0.34
ν_T	0.25	
α_A or α_m (ppm/°C)	-0.36	40.0
α_T (ppm/°C)	18.0	
σ_{my} (MPa)		100
$\sigma_{f,ult}$ (MPa)	3100	
Diameter (mm)	0.007	

3. Results

The previous section described a closed-form solution for the stresses around breaks in embedded single fibers. For a given applied stress, σ_{app}, and temperature differential, $T = T_s - T_0$, the complete stress state is defined by the ψ function. Specific components of the stress are defined in terms of ψ and its derivatives in Eqs. (46)–(51) and Eqs. (42)–(45). The required constants $\sigma_0(\rho)$, $\psi_0(\rho)$, and σ_∞ are defined in Eq. (80), Eq. (69), and Eq. (A4) in Appendix 1, respectively.

For a sample stress state, we consider a typical carbon fiber fragment with a length of 10 fiber diameters in an epoxy matrix. We use the fiber and matrix properties listed in Table I and arbitrarily choose $\sigma_0 =$ 25 MPa and $T = -125$°C. Finally, we need to select the radius of the inner two cylinders or, in other words, a value for V_2 — the volume fracture of the near-field matrix cylinder. We imagine at least three rational models for selecting V_2:

1. **Minimum Complementary Energy Model**: select V_2 to minimize the total complementary energy. Unfortunately this model fails because the minimum complementary energy occurs when $V_2 = 0$ or when the near-field matrix cylinder is eliminated.

2. **Matrix Plasticity Model**: An exact linear elastic stress analysis would show a stress singularity in the matrix at the crack tip of the fiber break. In real matrices, however, the matrix stress would not become singular but would be limited by the yield stress of matrix. The matrix plasticity model is to select V_2 such that the stress in the near-field matrix cylinder after the first fiber break is equal to the matrix yield stress—σ_{my}. After the first break, this model requires

$$\sigma_{zz,2} = \sigma_{my} = \frac{\sigma_0(\infty)}{V_2} \tag{89}$$

Before the first break we have

$$\sigma_{zz,2} = \sigma_{app} = \frac{\sigma_0(\infty) - V_1\psi_\infty}{V_2} \tag{90}$$

which allows us to determine $\sigma_0(\infty)$ and solve for V_2:

$$V_2 = \frac{\psi_\infty}{\psi_\infty + \sigma_{my} - \sigma_{app}} \tag{91}$$

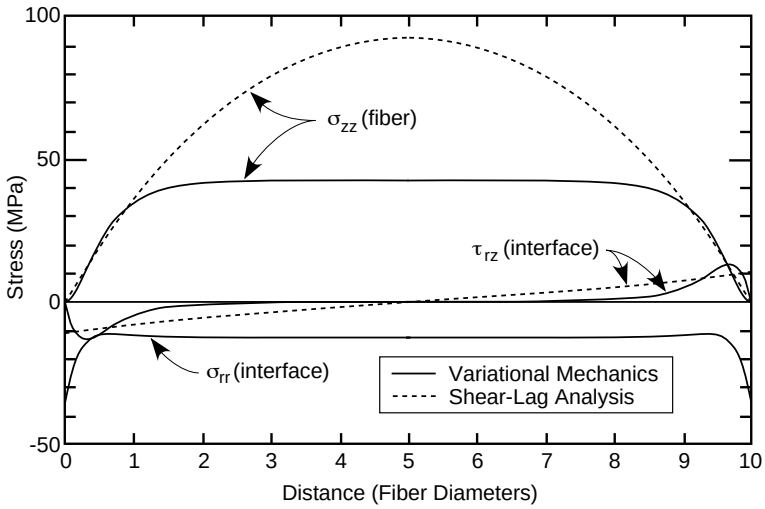

Fig. 4: The axial tensile stress in the fiber, σ_{zz}, the interfacial shear stress, τ_{rz}, and the interfacial radial stress, σ_{rr}, as a function of distance (in units of fiber diameters) in a fiber fragment of aspect ratio 10. The solid lines are the stresses calculated by the variational mechanics analysis. The dashed lines are the stresses calculated by a shear-lag analysis analysis.

3. **Experimentally Determined V_2 Model**: select V_2 such that the predicted fiber and matrix stresses agree with experimentally measured stresses. This model is discussed further below.

In the absence of experimental results for our hypothetical example, we resort to the matrix plasticity model. For the specific loading conditions of $\sigma_0 = 25$ MPa and $T = -125°$C, $\sigma_\infty = -12.53$ MPa, $\psi_\infty = 164.16$ MPa, and $\sigma_0(\infty) = 68.64$ MPa. By the matrix plasticity model we find $V_2 = 0.686$.

The solid lines in Fig. 4 plot the axial fiber stress and the shear and transverse stresses at the fiber/matrix interface. The axial fiber stress is zero at the fiber break, as required by boundary conditions, and builds to a constant plateau value within about three fiber diameters. For finite fiber fragment lengths, the plateau value is less than the far-field fiber stress of ψ_∞. This fiber fragment with an aspect ratio of 10 yields a plateau fiber stress that is 26% of the far-field fiber stress. The interfacial shear stress is zero at the fiber break, as required by boundary conditions, reaches a peak close to the fiber break, and then decays back to zero in about three fiber diameters. The interfacial radial stress shows a significant compressive stress concentration at the fiber break that is more than twice as large as the peak shear stress. The radial stress reaches a constant level of radial compression within about two fiber diameters. The constant level of radial compression is similar in magnitude to σ_∞. The large stress concentration is related, in part, to Poisson's contraction of the fiber. Near a fiber break, the fiber stress is low. This reduced stress causes a release of the fiber's Poisson's contraction and the fiber tries to expand against the bulk, uncracked matrix. The matrix prevents the expansion and a large compressive stress results. The compressive radial stress concentration at the fiber break should be expected to play a significant role in the mechanism of interfacial failure.

The dotted lines in Fig. 4 plot the axial fiber stress and the shear stress at the fiber/matrix interface calculated by the Cox (1952) shear-lag analysis (Eqs. (2) and (3)). The interfacial radial stress is not defined by shear-lag analysis. For the shear-lag calculations, the shear interaction parameter, H, is taken from Cox (1952) (see Eq. (5)). To account for thermal expansion, the applied strain in Eqs. (2) and (3) is

$$\varepsilon = \frac{\sigma_{app}}{E_m} + \alpha_m T \tag{92}$$

The shear-lag analysis stresses are significantly different than the variational mechanics analysis stresses.

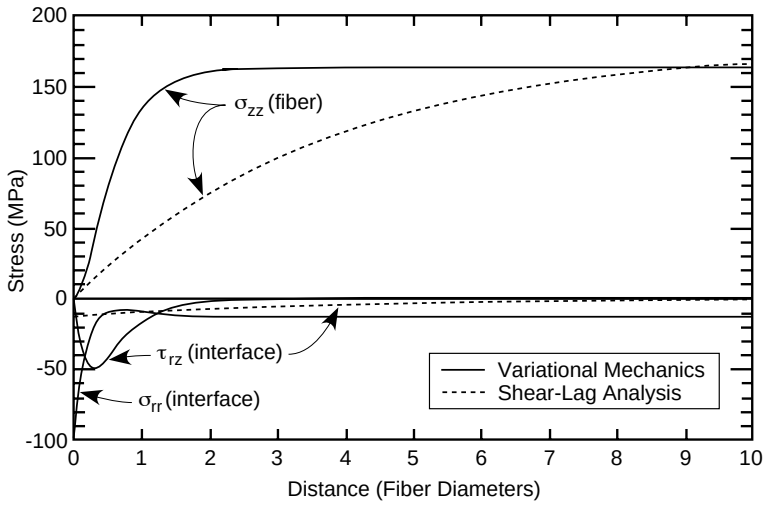

Fig. 5: The axial tensile stress in the fiber, σ_{zz}, the interfacial shear stress, τ_{rz}, and the interfacial radial stress, σ_{rr}, as a function of distance (in units of fiber diameters) from an isolated fiber break. The solid lines are the stresses calculated by the variational mechanics analysis. The dashed lines are the stresses calculated by a shear-lag analysis analysis.

The axial fiber stress increases at about the same rate near the fiber break, but continues to increase and peaks at a different maximum stress. The peak shear stress is similar in magnitude to the peak variational mechanics shear stress. The shear-lag shear stress, however, violates boundary conditions by being nonzero at the fiber break and decays more slowly towards zero. Agreement in maximum fiber axial stress can be improved by deviating from Cox's (1952) recommendations and choosing a lower value of H. Doing so, however, would worsen the agreement in the initial rate of axial stress increase and in the magnitude of the shear stresses.

Figure 5 plots the axial fiber stress and the shear and transverse stress at the fiber/matrix interface for an isolated fiber break. Again, the solid lines are the variational mechanics stresses and the dashed lines are the shear-lag analysis stresses. All stresses are similar in form to the stresses in a fiber fragment. The major difference is that in about three fiber diameters, all variational mechanics stresses approach the far-field stresses. In other words, σ_{zz}(fiber) approaches ψ_∞, σ_{rr}(interface) approaches σ_∞, and τ_{rz}(interface) approaches 0. The shear-lag analysis stresses are again significantly different than the variational mechanics analysis stresses. The shear-lag analysis predicts a much slower rate of increase in the axial fiber stresses and a lower magnitude of shear stress. Better agreement can be obtained by arbitrarily increasing the shear interaction parameter, H, but no value of H will give the correct form for the shear stress.

The are major differences between the variational mechanics analysis and the shear-lag analysis and we are compelled to consider the accuracy of the variational mechanics analysis. Figure 6 compares the variational mechanics analysis stresses to stresses calculated by an axisymmetric finite element analysis. To facilitate finite element calculations, the calculation is made for a finite two-cylinder specimen (*i.e.* $\sigma_{edge} = 0$ and $\sigma_0(\rho) = \sigma_{app}$). σ_{app}, T, and V_1 were arbitrarily chosen to be 25 MPa, -125°C, and 0.25, respectively. Because the variational mechanics stress analysis only calculates an average fiber stress, the plotted finite element stress is the average axial stress over the fiber cross-section. We find good agreement between variational mechanics stresses and finite element analysis stresses. Some minor fine structure in the finite element analysis near the fiber break may be due to insufficiently mesh refinement.

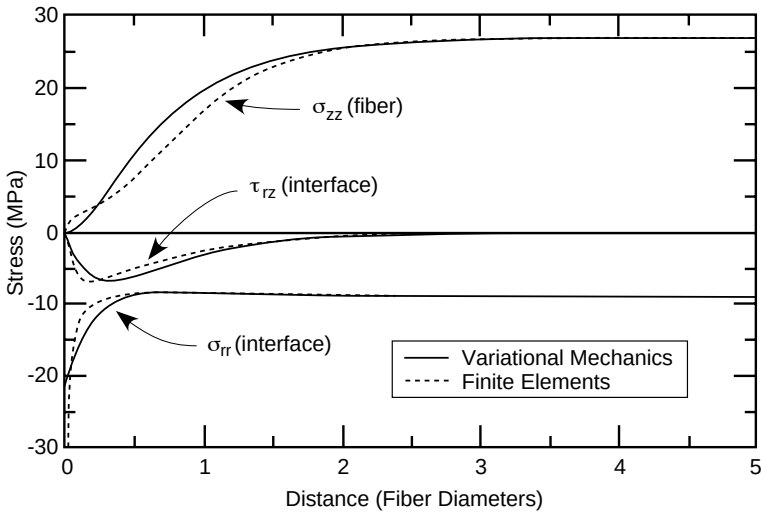

Fig. 6: The axial tensile stress in the fiber, σ_{zz}, the interfacial shear stress, τ_{rz}, and the interfacial radial stress, σ_{rr}, as a function of distance (in units of fiber diameters) from end of a two-cylinder fiber fragment of aspect ratio 10. The solid lines are the stresses calculated by the variational mechanics analysis. The dashed lines are the stresses calculated by an axisymmetric finite element analysis

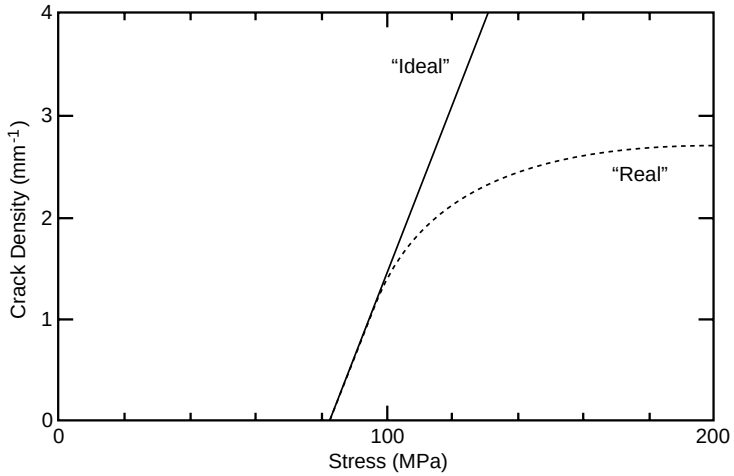

Fig. 7: The fiber crack density as a function of applied load for an "ideal" and a "real" single-fiber fragmentation test

For a fracture example, we plot predictions for an "ideal" single-fiber fragmentation test. By an "ideal" single-fiber fragmentation test, we mean a test on an embedded single fiber in which the interface is perfect and the fiber strength is given by a single invariant number denoted as $\sigma_{f,ult}$. The goal is to calculate the crack density as a function of applied load. For a given crack density, the maximum stress in the fiber is midway between two fiber breaks. The predicted crack density is thus found by numerically solving the equation

$$\sigma_{f,ult} = \psi_0(\rho)(1 - \phi(0)) \tag{93}$$

for crack density using incremental values of σ_{app}. The result using the fiber and matrix properties in Table I, $T = -125°\text{C}$, and $V_2 = 0.686$ is plotted in Fig. 7. The first crack forms at a stress of 83 MPa. For an infinite matrix sample, this stress corresponds to an applied strain of 1.93%. This strain is higher than the strain to failure of the fiber of 1.41% because of the initial thermal compressive strain of -0.50% caused by thermal shrinkage of the infinite matrix. After initial cracking, the crack density increases linearly with load.

"Real" single-fiber fragmentation tests always differ from the "ideal" test described in the previous paragraph. The two major causes of deviations are an imperfect interface and statistical variations in fiber strengths. An imperfect interface will cause the crack density to stop increasing and to level off at some plateau value (see "Real" test in Fig. 7). The plateau value defines a critical fragment length that has been used by many researches as a measure of the interfacial strength (Kelly and Tyson, 1963). The effect of statistical variations in fiber strengths will be to alter the overall shape of the crack density *vs.* applied load curve. Variations in fiber strength will at least change the slope of the curve and will probably also lead to non-linear results. While nearly all single-fiber fragmentation tests have focused only on the critical length, the manner in which the critical crack density is approached contains useful information about the mechanisms of interfacial failure and about statistical variations in fiber strengths. Hopefully the stress analysis described in this paper and the extensions mentioned in the discussion section will help extract this information from experimental results.

4. Discussion

We have described a new closed-form analysis for the stresses around breaks in embedded single fibers. The new analysis avoids limitations of previous analyses and by comparison to finite element calculations is seen to be accurate. The intention of this paper has only been to describe a new analysis procedure that can potentially serve as a tool for the interpretation of embedded single fiber tests. We choose this section to discuss some of the ways it might be used and some of the required extensions to handle new problems.

A logical starting point is to analyze "real" single-fiber fragmentation test results including results at sub-critical fragment lengths. The analysis of the "ideal" single-fiber fragmentation test was given in the previous section. To interpret "real" single-fiber fragmentation tests, we focus on three unresolved questions:

1. The near-field matrix cylinder volume fraction, V_2, needs to be realistically selected. Physically V_2 corresponds to the zone of matrix whose stresses are significantly affected by the presence of fiber breaks.

2. In the "ideal" single-fiber fragmentation test the fiber/matrix adhesion was assumed to be perfect; in "real" tests the adhesion will not be perfect. We need to account for interfacial failure and to describe the form of the stresses after interfacial failure.

3. In the "ideal" single-fiber fragmentation test the fiber was assumed to have a unique tensile strength; "real" fibers will have a statistical distribution of strengths.

The first question about defining V_2, is best answered using the "Experimentally Determined V_2 Model." When the fiber is intact, the stresses calculated are independent of V_2. When the fiber contains breaks, however, the predicted stresses will depend on V_2. By comparing predicted stresses as a function of V_2 to measured stresses, it should be possible to experimentally measure V_2. Two experimental techniques are available. The first is photoelasticity of a birefringent matrix (Drzal, Rich and Lloyd, 1982; Drzal, Rich, Koenig and Lloyd, 1983; Drzal, Rich and Koenig, 1985; Rich and Drzal, 1986; Bascom and Jensen, 1986). The photoelastic fringes caused by stresses in the matrix can be compared to calculated fringes derived from stresses found using various values of V_2. A second, complementary approach is to measure the fiber stresses using Raman spectroscopy (Galiotis and Jahankhani, 1988; Robinson, Zakikhani, Day and Young, 1987) and

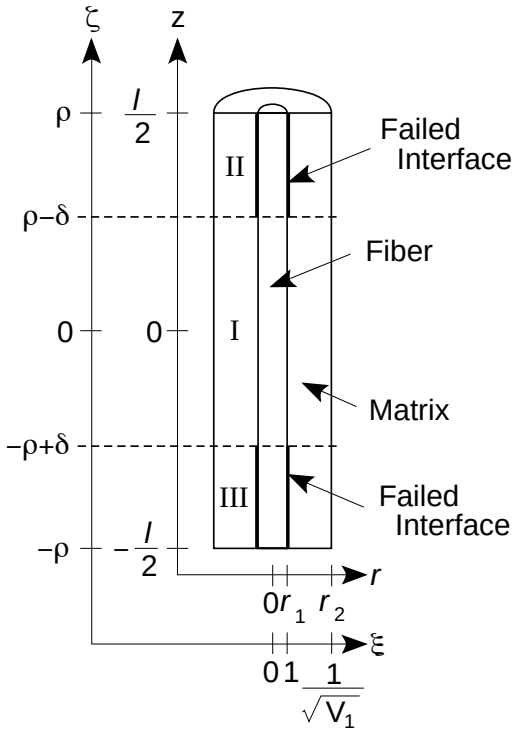

Fig. 8: A single fiber fragment of length l showing three regions. Region I has an intact fiber/matrix interface while regions II and III have failed fiber/matrix interfaces. The regions of failed interface are δ dimensionless units long.

compare them to predicted fiber stresses as a function of V_2.

An alternative approach is to eliminate the need for a third cylinder by using a more refined variational mechanics analysis. The refined analysis must relax the assumption that the axial stress in the matrix cylinder is independent of r. For example, an alternative matrix stress function might be

$$\Psi(r,z) = \frac{r^2}{4}\left[\sigma_{app} + \psi_0(z)\left(\frac{2}{\lambda+2}\right)^2 r^\lambda\right] + \psi_1(z)\ln r + \psi_2(\zeta) \tag{94}$$

This stress function gives the matrix axial stress as

$$\sigma_{zz,2} = \sigma_{app} + \psi_0(z) r^\lambda \tag{95}$$

When $\lambda < 0$ the axial stress approaches the far-field matrix stress away from the fiber break. The price of the improved stress function is to considerably complicate the mathematical analysis and it is hoped to address this problem in future work.

We deal with the second question about imperfect adhesion by adding regions containing failed fiber/-matrix interfaces. The new problem requiring analysis is illustrated in Fig. 8. Region I has an intact fiber/-matrix interface and regions II and III, both of dimensionless length δ, have failed fiber/matrix interfaces. The stress analysis in region I can be completed by procedures identical to those outlined in this paper. The stress analyses in regions II and III require new techniques. Despite the post-failure nature of the stresses in regions II and III, those stresses must still obey equilibrium. Thus, the form of the region II and III stresses must still be given by Eqs. (46)–(51) and Eqs. (42)–(45) and the problem of finding the stresses is reduced to finding ψ. We suggest a good starting point is to assume some form of the interfacial stresses such as

$$\tau_{rz}(1) = \mu\sigma_{rr}(1) + \tau_y \tag{96}$$

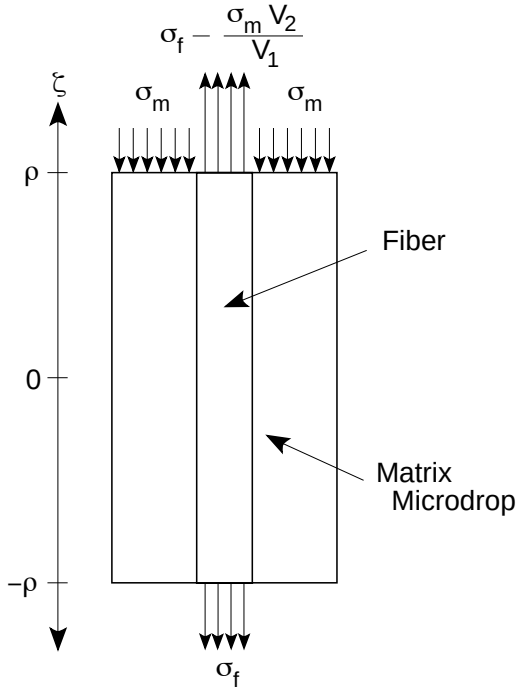

Fig. 9: A matrix microdrop of dimensionless length 2ρ showing the boundary conditions relevant to the microdrop debond test. σ_f is the background fiber tensile stress. σ_m is the stress applied to the microdrop during the test.

In Eq. (96), the first term is a frictional term with μ the coefficient of friction. This term only makes sense when the radial stresses are compressive. It may also be necessary to adjust μ for slip or stick frictional effects. The second term is an interfacial shear yield stress similar in intent to the simple Kelly and Tyson (Kelly and Tyson, 1963) shear-yield stress. Inserting the form of the equilibrium stresses into Eq. (96) results in a second order differential equation for the ψ function:

$$\mu f_1(1)\psi'' + \frac{1}{2}\psi' - \frac{\mu V_2 A_3}{V_1 A_0}\psi = \frac{\mu V_2}{V_1}\left(\frac{A_4\sigma_0(\rho)}{A_0} + \frac{A_5 T}{A_0}\right) - \mu\sigma_\infty\left(1 - \frac{V_2 A_2}{V_1 A_1}\right) - \tau_y \tag{97}$$

The boundary conditions for Eq. (97) are $\psi(\rho) = \psi'(\rho) = 0$ in region II and $\psi(-\rho) = \psi'(-\rho) = 0$ in region III. Solving Eq. (97) for ψ determines all the stresses in regions II and III. The analysis of region I is virtually identical to the analysis in this paper. There are two minor changes. First, the boundary conditions will be different. The values of $\psi(\pm(\rho-\delta))$ and $\psi'(\pm(\rho-\delta))$ will no longer be zero but will be determined by the stress state in regions II and III. Second, because in general $\psi'(\pm(\rho-\delta)) \neq 0$, the observation that $\langle\psi''\rangle = 0$, used when calculating $\sigma_0(\rho)$ and $\langle\phi\rangle$, is no longer valid and the terms involving $\langle\psi''\rangle$ will have to be carried through the analysis.

An important application of the stress analysis that includes a failed interface is to study the mechanism of interfacial failure. In other words, what stress conditions cause the extent of interfacial failure or the lengths of regions II and III to increase? Due to the complexity of the multiaxial stress state, it seems unlikely that a simple maximum stress failure criterion will be realistic. We would suggest an energy release rate analysis. With a completed stress analysis, it is possible to calculate the total energy release rate associated with the growth of interfacial damage. Comparison of predictions to experiments should reveal if a critical interfacial toughness can be used to predict the onset and propagation of interfacial damage.

The third question about dealing with distributions of fiber strengths can be handled in various ways.

In general, we will have to develop a stochastic model based on some assumed or measured distribution of fiber flaws. Given a description of fiber flaws and their strengths, a stress analysis of fiber fragments of various lengths can be used to predict the probability of failure as a function of applied load. It would then be possible to develop a computer model to predict the average fiber fragment length as well as the distribution of fiber fragment lengths as a function of applied load. Such a computer model coupled with a model for imperfect adhesion could be expected to reproduce many of the features of "real" single-fiber fragmentation tests.

Although we have concentrated on the single-fiber fragmentation test, we note that simple changes in boundary conditions can be used to effect stress analyses of other single-fiber tests such as the microdrop debond test (Gaur and Miller, 1989) and the fiber pull-out test (Piggot, Chua and Andison, 1985). To be specific, we consider the microdrop debond test. In the microdrop debond test, a microdrop of matrix is applied to a fiber and the force required to slide the drop along the fiber or to break the fiber/matrix interface is measured. The force is applied directly to the matrix microdrop using micrometer adjusted knife edges. If we replace the microdrop by an effective cylinder of length 2ρ and ignore the third far-field matrix cylinder, the microdrop debond specimen can be analyzed by solving the problem illustrated in Fig. 9. Before loading the matrix microdrop the fiber has a background stress of σ_f. During the test, the matrix microdrop is directly loaded with a compressive stress σ_m. This stress on the matrix causes the stress on the fiber at $\zeta = \rho$ to increase by an amount $-\frac{\sigma_m V_2}{V_1}$. For the microdrop debond specimen, the boundary conditions on the ψ function are thus $\psi(-\rho) = \sigma_f$, $\psi(\rho) = \sigma_f - \frac{\sigma_m V_2}{V_1}$, and $\psi'(\pm\rho)$=0. The total applied stress is $\sigma_0 = V_1\sigma_f$. Reworking the analysis in this paper with these new boundary conditions results in a new analysis of the microdrop debond test (Scheer and Nairn, 1992). Similar types of changes in boundary conditions can be used to analyze other types of embedded single fiber tests.

Acknowledgments

This work was supported in part by a contract from NASA Langley Research Center (NAS1-18833) monitored by Dr. John Crews, and in part by a gift from the Fibers Department of E. I. duPont deNemours & Company monitored by Dr. Alan R. Wedgewood. The author also thanks Dr. Willard D. Bascom for many helpful discussions.

References

Amirbayat, J. and W. S. Hearle (1969), Properties of unit composites as determined by the properties of the interface. Part I: Mechanism of matrix-fibre load transfer, *Fiber Sci. and Tech.*, **2**, 123.

Bascom, W. D. and R. M Jensen. (1986), Stress transfer in single fiber/resin tensile tests, *J. Adhesion*, **19**, 219.

Broutman, L. J. and B. D. Agarwal (1974), A theoretical study of the effect of an interfacial layer on the properties of composites, *Polym. Eng.& Sci.*, **14**, 581.

Carlson, D. M. (1984), Linear Thermoelasticity, in: C. Truesdall, ed., *Mechanics of Solids: Volume II*, Springer-Verlag, Berlin, p. 325.

Carrara, A. S. and F. J. McGarry (1968), Matrix and interface stresses in a discontinuous fiber composite model, *J. Comp. Mat.*, **2**, 222.

Cox, H. L. (1952), The elasticity and strength of paper and other fibrous materials, *Brit.J. Appl. Phys.*, **3**, 72.

DiBenedetto, A. T. and P. J. Lex (1989), Evaluation of surface treatments for glass fibers in composite materials, *Polymer Composites*, **29**, 543.

DiLandro, L. and M. Pegoraro (1987), Carbon fiber–thermoplastic matrix adhesion, *J. Mat. Sci.*, **22**, 1980.

DiLandro, L., A. T. DiBenedetto and J. Groeger (1988), The effect of fiber-matrix stress transfer on the strength of fiber-reinforced composite materials, *Polymer Composites*, **9**, 209.

Drzal, L. T., M. J. Rich, J. D. Camping and W. J. Park (1980), Interfacial shear strength and failure mechanisms in graphite fiber composites, *Proc. 35th Conf. SPI Reinforced Plastics Div.*, **Section 20-C**, 1.

Drzal, L. T., M. J. Rich and P. F Lloyd (1982), Adhesion of graphite fibers to epoxy matrices: I. The role of fiber surface treatment, *J. Adhesion*, **16**, 1.

Drzal, L. T., M. J. Rich, M. F Koenig and P. F. Lloyd (1983), Adhesion of graphite fibers to epoxy matrices: II. The effect of fiber finish, *J. Adhesion*, **16**, 133.

Drzal, L. T., M. J. Rich and M. F. Koenig (1985), Adhesion of graphite fibers to epoxy matrices: III: The effect of hygrothermal exposure, *J. Adhesion*, **18**, 49.

Folkes, M. J. and W. K. Wong (1987), Determination of interfacial shear strength in fibre-reinforced thermoplastic composites, *Polymer*, **28**, 1309.

Fraser, A. A., F. H. Ancker and A. T. DiBenedetto (1975), A computer modeled, single filament technique for measuring coupling and sizing agent effects in fiber reinforced composites, *Proc. 30th Conf. SPI Reinforced Plastics Div.*, **Section 22-A**, 1.

Fraser, W. A., F. H Ancker, A. T. DiBenedetto and B. Elbirli (1983), Evaluation of surface treatments for fibers in composite materials, *Polym. Comp.*, **4**, 238.

Galiotis, C. and H. Jahankhani (1988), Interfacial studies on a Kevlar® 49/epoxy system in tension and compression, in: H. Ishida, ed., *Interfaces in Polymer, Ceramic, and Metal Matrix Composites (ICCI-II)*, Elsevier Sci. Publ. Co., London, p. 107.

Garret, K. W. and J. E. Bailey (1977), Multiple transverse fracture in 90° cross-ply laminates of a glass fibre-reinforced polyester, *J. Comp. Mat.*, **12**, 157.

Gaur, U. and B. Miller (1989), Microbond method for determination of the shear strength of a fiber/resin interface: evaluation of experimental parameters, *Comp. Sci. & Tech.*, **34**, 35.

Hahn, H. T. and S. W. Tsai (1974), On the behavior of composite laminates after initial failures, *J. Comp. Mat.*, **8**, 288.

Hashin, Z. (1985), Analysis of cracked laminates: a variational approach, *Mechanics of Materials*, **4**, 121.

Hashin, Z. (1986), Analysis of stiffness reduction of cracked cross-ply laminates, *Eng. Fract. Mech.*, **25**, 771.

Highsmith, A. L. and K. L. Reifsnider (1982), Stiffness-reduction mechanisms in composite laminates, *ASTM STP*, **775**, 103.

Kelly, A. and W. R. Tyson (1963), Fibre-strengthened materials, *J.Mech. Phys. Solids*, **10**, 199.

Liu, S. and J. A. Nairn (1990), Fracture mechanics analysis of composite microcracking: experimental results in fatigue, *Proceedings of the Fifth Annual Meeting of the American Society of Composites*, , 287.

Liu, S. and J. A Nairn. (1992), The formation and propagation of matrix microcracks in cross-ply laminates during static loading, *J. Reinf. Plast. & Comp.*, , in press.

Mandell, J. F., E. J. H. Chen and F. J. McGarry (1980), A microdebonding test for *in situ* assessment of fiber/matrix bond strength in composite materials, *Intl. J. Adhes. Adhes.*, **1**, 40.

Nairn, J. A. (1985), Thermoelastic analysis of residual stresses in unidirectional, high-performance composites, *Polym. Comp.*, **6**, 123.

Nairn, J. A. (1989), The strain energy release rate of composite microcracking: a variational approach, *J. Comp.Mat.*, **23**, 1106. (*Errata* published as *J. Comp. Mat.*, **24**, 233 (1990)).

Netravali, A. N., P. Schwartz and S. L. Phoenix (1989), Study of interfaces of high-performance glass fibers and DGEBA-based epoxy resins using single-fiber-composite test, *Polymer Composites*, **10**, 385.

Ohsawa, T., A. Nakayama, M. Miwa and A. Hesegawa (1978), Temperature dependence of critical fiber length for glass fiber-reinforced thermosetting resins, *J. Appl. Polym. Sci.*, **22**, 3203.

Penn, L. S., F. A. Bystry and H. J. Marchionni (1983), Relation of interfacial adhesion in Kevlar®/epoxy systems to surface characterization and composite performance, *Polymer Composites*, **4**, 26.

Piggot, M. R., P. S. Chua and D. Andison (1985), The interface between glass and carbon fibers and thermosetting polymers, *Polymer Composites*, **6**, 242.

Piggot, M. R. (1987), Debonding and friction at fiber-polymer interfaces. I: Criteria for failure and sliding, *Comp. Sci. & Tech.*, **30**, 295.

Rich, M. J. and L. T. Drzal (1986), Interfacial properties of some high-strain carbon fibers in an epoxy matrix, *Proc. 41st Conf. SPI Reinforced Plastics Div.*, **Section 2-F**, 1.

Robinson, I. M., M. Zakikhani, R. J. Day and R. J. Young (1987), Stain dependence of the raman frequencies for different types of carbon fibers, *J. Mat. Sci.*, **6**, 1212.

Rosen, B. W. (1964), Mechanics of composite strengthening, in: *Fiber Composite Materials*, American Society of

Metals, Metals Park, Ohio, Ch. 3, p. 37.
Scheer, R. J. and J. A. Nairn (1992), Variational Mechanics Analysis of Stresses and Failure in Microdrop Debond Specimens, *Composites Engineering*, , in press.
Timoshenko, S. P. and J. N. Goodier (1970), *Theory of Elasticity*, McGraw-Hill Book Company, New York.
Wadsworth, N. J. and I. Spilling (1968), Load transfer from broken fibres in composite materials, *Brit. J. Appl. Phys. (J. Phys. D.)*, **1**, 1049.
Whitney, J. M. and L. T. Drzal (1987), Axisymmetric stress distribution around an isolated fiber fragment, *Toughened Composites*, **ASTM STP 937**, 179.

Appendix 1. Elasticity Analyses When Fiber has No Breaks

We present an elasticity analysis for an infinitely long fiber with no breaks. We begin with a two-cylinder model under total axial stress σ_0 and constant radial stress σ_{edge}. In the exact elasticity solution all shear stresses will be zero and σ_{zz} will be independent of ξ within each cylinder. We can thus recover the form of the exact solution by using Eqs. (46)–(51) with $\psi' = \psi'' = 0$. The result is

$$\begin{aligned} \sigma_{zz,1} &= \psi_0 & \qquad \sigma_{zz,2} &= \frac{\sigma_0 - V_1\psi_0}{V_2} \\ \sigma_{rr,1} = \sigma_{\theta\theta,1} &= -\frac{V_2}{V_1}\psi_6 + \sigma_{edge} & \qquad \sigma_{rr,2} &= \psi_6\left(1 - \frac{1}{\xi^2 V_1}\right) + \sigma_{edge} \\ & & \qquad \sigma_{\theta\theta,2} &= \psi_6\left(1 + \frac{1}{\xi^2 V_1}\right) + \sigma_{edge} \end{aligned} \tag{A1}$$

where the two unknowns ψ_0 and ψ_6 are constants. We determine ψ_0 and ψ_6 using two conditions. First, the axial strain (ε_{zz}) in the fiber and the matrix are equated. Second, the radial displacements ($u = r\varepsilon_{\theta\theta}$) at the fiber matrix interface are equated. The result is

$$\begin{aligned} \psi_0 = \frac{1}{C_{33}}\Bigg\{ &\left[\frac{1}{2V_2E_m} + \frac{V_2A_3A_4}{V_1A_0}\right]\sigma_0 + \left[\frac{1}{2}(\alpha_m - \alpha_A) + \frac{V_2A_3A_5}{V_1A_0}\right]T \\ &+ \left[\frac{\nu_A}{E_A} - \frac{\nu_m}{E_m} + \frac{V_2A_3A_2}{V_1A_0}\right]\sigma_{edge}\Bigg\} \end{aligned} \tag{A2}$$

$$\begin{aligned} \psi_6 = \frac{1}{C_{33}}\Bigg\{ &\left[\frac{A_3}{2A_0V_2E_m} + \frac{A_4}{2A_0}\left(\frac{1}{E_A} + \frac{V_1}{V_2E_m}\right)\right]\sigma_0 + \left[\frac{A_3(\alpha_m - \alpha_A)}{2A_0} + \frac{A_5}{2A_0}\left(\frac{1}{E_A} + \frac{V_1}{V_2E_m}\right)\right]T \\ &+ \left[\frac{A_3}{A_0}\left(\frac{\nu_A}{E_A} - \frac{\nu_m}{E_m}\right) + \frac{A_2}{2A_0}\left(\frac{1}{E_A} + \frac{V_1}{V_2E_m}\right)\right]\sigma_{edge}\Bigg\} \end{aligned} \tag{A3}$$

This elasticity result for ψ_0 is identical to the variational analysis solution for $\psi_0(\rho)$ in Eq. (69).

To find σ_∞ and ψ_∞ we set $\sigma_{edge} = 0$, pass to the limit as $V_1 \to 0$, and note that $\sigma_\infty = -\frac{V_2}{V_1}\psi_6$. The result of this exercise is

$$\sigma_\infty = \frac{(\nu_m - \nu_A)\frac{\sigma_0}{E_m} + \big(\nu_A(\alpha_A - \alpha_m) + (\alpha_T - \alpha_m)\big)T}{\frac{2\nu_A^2}{E_A} - \frac{1-\nu_T}{E_T} - \frac{1+\nu_m}{E_m}} \tag{A4}$$

$$\psi_\infty = \frac{\left(\frac{2\nu_A\nu_m}{E_A} - \frac{1-\nu_T}{E_T} - \frac{1+\nu_m}{E_m}\right)\frac{E_A\sigma_{app}}{E_m} + \left(\frac{2\nu_A}{E_A}(\alpha_T - \alpha_m) + \left(\frac{1-\nu_T}{E_T} + \frac{1+\nu_m}{E_m}\right)(\alpha_A - \alpha_m)\right)E_AT}{\frac{2\nu_A^2}{E_A} - \frac{1-\nu_T}{E_T} - \frac{1+\nu_m}{E_m}} \tag{A5}$$

Although it is not obvious that Eq. (5) is identical to the variational analysis result for ψ_∞ (Eq. (72)), their identity can be verified numerically or by tortuous algebra.

Appendix 2. Solution When $\frac{p^2}{4} - q < 0$

When $\frac{p^2}{4} - q < 0$, the solution to the Euler equation (Eq. (2.75)) is

$$\phi = \frac{2h_2'(\rho)\cosh\alpha\zeta\cos\beta\zeta - 2h_1'(\rho)\sinh\alpha\zeta\sin\beta\zeta}{\beta\sinh 2\alpha\rho + \alpha\sin 2\beta\rho} \tag{A6}$$

where

$$h_1(\rho) = \cosh\alpha\rho\cos\beta\rho \tag{A7}$$

$$h_2(\rho) = \sinh\alpha\rho\sin\beta\rho \tag{A8}$$

$$\alpha = \frac{1}{2}\sqrt{2\sqrt{q} - p} \tag{A9}$$

$$\beta = \frac{1}{2}\sqrt{2\sqrt{q} + p} \tag{A10}$$

The derivatives of ϕ and the $\chi(\rho)$ function become

$$\phi' = \frac{2\Big(\alpha h_2'(\rho) - \beta h_1'(\rho)\Big)\sinh\alpha\zeta\cos\beta\zeta - 2\Big(\beta h_2'(\rho) + \alpha h_1'(\rho)\Big)\cosh\alpha\zeta\sin\beta\zeta}{\beta\sinh 2\alpha\rho + \alpha\sin 2\beta\rho} \tag{A11}$$

$$\phi'' = \frac{2\Big((\alpha^2-\beta^2)h_2'(\rho) - 2\alpha\beta h_1'(\rho)\Big)\cosh\alpha\zeta\cos\beta\zeta - 2\Big(2\alpha\beta h_2'(\rho) + (\alpha^2-\beta^2)h_1'(\rho)\Big)\sinh\alpha\zeta\sin\beta\zeta}{\beta\sinh 2\alpha\rho + \alpha\sin 2\beta\rho} \tag{A12}$$

$$\chi(\rho) = 2\alpha\beta(\alpha^2+\beta^2)\frac{\cosh 2\alpha\rho - \cos 2\beta\rho}{\beta\sinh 2\alpha\rho + \alpha\sin 2\beta\rho} \tag{A13}$$

The solution for an isolated crack is (Hashin, 1985):

$$\psi = \psi_\infty\left[1 - e^{-\alpha\zeta}\left(\cos\beta\zeta + \frac{\alpha}{\beta}\sin\beta\zeta\right)\right] \tag{A14}$$

$$\psi' = \psi_\infty\left(\frac{\alpha^2+\beta^2}{\beta}\right)e^{-\alpha\zeta}\sin\beta\zeta \tag{A15}$$

$$\psi'' = \psi_\infty\left(\alpha^2+\beta^2\right)e^{-\alpha\zeta}\left(\cos\beta\zeta - \frac{\alpha}{\beta}\sin\beta\zeta\right) \tag{A16}$$